Journal of The Electrochemical Society

OPEN ACCESS

Editors' Choice—4D Neutron and X-ray Tomography Studies of High Energy Density Primary Batteries: Part I. Dynamic Studies of $LiSOCl_2$ during Discharge

To cite this article: Ralf F. Ziesche *et al* 2020 *J. Electrochem. Soc.* **167** 130545

Journal of The Electrochemical Society, 2020 **167** 130545

Editors' Choice—4D Neutron and X-ray Tomography Studies of High Energy Density Primary Batteries: Part I. Dynamic Studies of $LiSOCl_2$ during Discharge

Ralf F. Ziesche,[1,2,3,4] James B. Robinson,[1,2] Matthew D. R. Kok,[1,2] Henning Markötter,[5,6,7] Winfried Kockelmann,[4] Nikolay Kardjilov,[5] Ingo Manke,[5] Dan J. L. Brett,[1,2] and Paul R. Shearing[1,2,z]

[1]*Electrochemical Innovation Lab, Department of Chemical Engineering, UCL, London, WC1E 7JE, United Kingdom*
[2]*The Faraday Institution, Quad One, Harwell Science and Innovation Campus, Didcot, OX11 0RA, United Kingdom*
[3]*Diamond Light Source Ltd., Harwell Science and Innovation Campus, Didcot, OX 11 0DE, United Kingdom*
[4]*STFC, Rutherford Appleton Laboratory, ISIS Facility, Harwell, OX11 0QX, United Kingdom*
[5]*Helmholtz-Zentrum Berlin für Materialien und Energie (HZB), Berlin, 14109, Germany*
[6]*Technische Universität Berlin, Berlin, 10624, Germany*
[7]*Bundesanstalt für Materialforschung und -Prüfung, Berlin,12205, Germany*

The understanding of dynamic processes in Li-metal batteries is an important consideration to enable the full capacity of cells to be utilised. These processes, however, are generally not directly observable using X-ray techniques due to the low attenuation of Li; and are challenging to visualise using neutron imaging due to the low temporal resolution of the technique. In this work, complementary X-ray and neutron imaging are combined to track the dynamics of Li within a primary $Li/SOCl_2$ cell. The temporal challenges posed by neutron imaging are overcome using the golden ratio imaging method which enables the identification of Li diffusion *in operando*. This combination of techniques has enabled an improved understanding of the processes which limit rate performance in $Li/SOCl_2$ cells and may be applied beyond this chemistry to other Li-metal cells.
 [DOI: 10.1149/1945-7111/abbbbc]

Manuscript submitted August 5, 2020; revised manuscript received September 9, 2020. Published October 15, 2020.

Lithium batteries have transformed energy storage technology due to their significant advantages in comparison to other cell chemistries, including their high cell voltage, comparatively lightweight nature of the cells, long cycle life and high capacity and rate performance. These characteristics have enabled Li cells to be deployed in applications as varied as portable electrical devices, medical implants,[1] automotive powertrains[2] or for applications in space.[3] Primary Li cells have historically been preferred for long-duration backup power due to their outstanding shelf-life, high potential and capacity. One of the most common cell chemistries for such applications is the Limetal vs thionyl chloride ($SOCl_2$)[4–7] cell which is also suitable for applications under extreme conditions including very low or high temperatures.[8,9] $Li/SOCl_2$ primary batteries are mainly available in two cell designs: the bobbin configuration, investigated in that manuscript, and as a spirally wound cell. Bobbin type cells, while low cost and relatively simple to manufacture, can show a fundamental capacity loss at higher discharge rates. A number of different factors can prematurely interrupt the cell operation, such as the loss of the electrical or ionic conductivity of the electrodes. An improved understanding of mechanisms which lower the cell capacity and lifetime is crucial for designing improved batteries.

Three-dimensional (3D) and four-dimensional (4D) imaging, i.e. 3D spatially and temporally resolved methods such as X-ray computed tomography (CT), are powerful tools to track processes which affect battery performance. The high spatial and time resolution which range from the millimetre to the nanometre length scale,[10] exposure times of fractions of a second to acquire radiographic images[11,12] and as little as several seconds for full CTs[13–15] enable the study of the battery architecture, electrode microstructure, new battery materials and battery safety. The high sensitivity to high-Z elements provides a good imaging contrast for metallic materials such as the anode and cathode current collectors, and the active electrode materials such as $LiMnO_2$,[15] LCO,[16] LFP[17] or NMC.[18] However, light elements such as lithium appear transparent when imaged with X-rays, in the "tender" or hard X-ray energy spectrum. In contrast, neutrons show a high sensitivity for some low-Z elements providing a high contrast for both lithium and hydrogen. In contrast, some metals such as lead have low attenuation coefficients when imaged using neutrons. This is a consequence of X-rays interacting with the electron cloud with the attenuation coefficient increasing with a rising Z, whereas neutrons interact with the nucleus and provide different attenuation coefficients even between isotopes of the same element. Recently, neutrons have demonstrated significant potential in imaging electrochemical devices, for example, for visualising the water evolution in fuel cells[19–21] and electrolysers,[22,23] to examine dynamic Li diffusion processes and electrode expansion,[24–27] electrolyte consumption[28] and gas evolution[29–31] in Li batteries. However, neutron imaging is often limited to radiography and suffers from poor spatial resolution and long exposure times due to the characteristically low flux available at most neutron sources. This makes it challenging to image dynamic processes at high-resolution. Recent developments have shown an improved speed in neutron CT collection[32,33] and spatial resolutions down to a few micrometres[34–36] are achievable, which in turn has increased the potential to track dynamic lithium diffusion processes in lithium batteries.

In cases where dynamic processes are slow, neutron sources with a lower flux can perform 4D studies by using an appropriate spatio-temporal scanning strategy, such as the golden-ratio (GR) scanning method. Conventional tomographic reconstruction techniques require projections in sequences of equal angular distances. The spatial and temporal resolution is predetermined and cannot be changed during the measurements or afterwards. Additionally, if one of the sequential projections is missing or defective, caused by problems with the camera system or an interruption of the radiation, the data cannot be reconstructed or will contain significant artefacts. In the case of a static sample the missing projections can be repeated, or fluctuations of the neutron flux can be monitored and balanced by the variation of the exposure time. However, replacing lost projections is not possible for dynamic processes. The mathematical background and a demonstration of the GR technique is shown by Kaestner et al.[37] This scanning strategy is based on non-sequential decompositions of the sample rotation angle sequence. The organisation of the projections by using

[z]E-mail: p.shearing@ucl.ac.uk

the golden-ratio was first introduced by Köhler,[38] who organised the projections by using the GR (shown in Eq. 1) to calculate the optimal acquisition angle of each projection such as shown in Eq. 2 for a tomographic scan over 180° with n the number of the projections.

$$g = \frac{\sqrt{5} - 1}{2} \approx 0.618 \quad [1]$$

$$GR\ \ angle(n) = g \cdot n \cdot 180^\circ\ \ mod\ \ 180^\circ | n\ \epsilon\ \mathbb{Z}_0^+ \quad [2]$$

The next angle is centred in the biggest gap of the previously acquired angles to minimise the overlap of the completed projections and prevent redundant information. Using this method, a time-resolved data set is achieved by using a certain set of consecutive projections, possibly with a high overlap of the projections between consecutive tomographies in a running-average mode. For an improvement in spatial resolution, a larger number of consecutive projections is used and the projection overlap can be reduced.

The combination of both non-destructive neutron and X-ray CT techniques provides opportunities to combine structural information such as particle movements, obtained from the X-rays, with electrochemical information such as lithium diffusion or the lithium content change in the cathode or anode, obtained from the neutrons. The successful combination of X-ray and neutron CT on batteries was for the first time demonstrated by LaManna et al.[39] This combination of complementary imaging techniques enables the study of the dynamic processes inside batteries in 4D and provides opportunities to deliver new insights in processes which occur simultaneously such as e.g. Li diffusion and electrode expansion.[40]

Experimental

1200 mAh LS 14250 Li/$SOCl_2$ cells (Saft Groupe A.A., France) were examined to understand the rate-dependent structural changes using a combination of X-ray and neutron imaging. The LS 14250 cell is a ½ AA sized commercial Li/$SOCl_2$ battery with an internal bobbin type structure designed for low-rate applications such as backup batteries in computers or burglar alarm systems. This low-cost, primary cell type provides a nominal voltage of 3.6 V at room temperature with a flat discharge profile over a long-time range and can operate over a wide temperature range of –60 °C to +85 °C, with a very low self-discharge rate, which makes the cell chemistry a popular choice for applications in extreme conditions.[5,41] Figure 1a shows the schematic drawing of the internal structure of a bobbin type Li/$SOCl_2$ battery cell. The liquid $SOCl_2$ cathode (green) in the middle of the cell is surrounded by the lithium-metal negative electrode (grey) and separated by a separator layer (yellow) soaked in a $SOCl_2$:$LiAlCl_4$ non-aqueous electrolyte (blue). A porous supporting carbon skeleton surrounds the liquid cathode providing an enhanced electrical conductivity. A cathode current collector rod (grey) in the centre of the cell connects this porous carbon to the positive tab. The lithium anode is directly connected to the cell can which acts as the negative terminal. During cell discharge Li-ions move from the Li anode into the electrolyte, diffuse through the Li^+ permeable separator layer to the cathode side and react with the $SOCl_2$ to form LiCl, SO_2 gas and solid sulphur.

Two LS 14250 cells were discharged under constant current conditions at 25 mA and 8 mA, respectively. Both of these discharge currents are below the maximum recommended discharge current of 35 mA, however, these rates are known to result in a significant loss of usable capacity, as detailed in the cell data sheet.

Time resolved neutron CT scans at a 25 mA discharge current were performed at the V7 CONRAD-2 neutron imaging beamline[42,43] at the BER II research reactor at the Helmholtz Zentrum Berlin. CONRAD-2 is optimised for high spatial and time resolved neutron imaging. The intermediate measuring position of CONRAD-2 was used to maximize the high neutron flux at an acceptable spatial resolution. This position was equipped with a high speed, indirect detector system including a 200 μm thick ^{6}LiF/ZnS:Ag scintillator screen for a high neutron to light conversion efficiency and a cooled −30 °C sCMOS "Neo" camera from Oxford Instruments/Andor (UK) which provides a high frame rate with short readout delays. Both components were used in combination with a bright Nikon photo lens (f = 50 mm, aperture 1.2) to reduce the light losses inside the camera box and focus the object on to the camera photo chip. For an optimal L/D ratio a 3 cm pinhole configuration was selected, positioned about 5 m in the front of the detector system at the end of the NL-1B neutron guide. The LS 14250 cell was mounted in front of the scintillator screen on an adjustable stick on the V7 rotation stage (Goniometer 409, Huber Diffraktiontechnik, Germany) by a stainless steel clip. With a calculated L/D of about 167, the spatial resolution was about 150 μm with a pixel size of 55 μm. Before the cell was secured onto the sample holder the plastic coating was removed to mitigate the contribution of this layer to neutron scattering. The electrical connection to the GAMRY 1000E potentiostat (GAMRY Instruments, USA) was maintained by a stainless steel clip at the electrical negative cell can and a crocodile clip at the top positive terminal tab. The battery was discharged in constant current mode at 25 mA. During discharging, continuous neutron radiographies were collected with an exposure time of 2 s per image by the Andor Solis software. Tomograms were sequentially accumulated during 360° rotation with 600 projections acquired for each full tomography in approximately 20 min. Every hour, two tomographies were performed whereby the first was acquired through a counter-clockwise rotation and the second clockwise; labelled as forward and backward respectively. Figure 1b shows an example of a 3D data set with an illustration of the rotation conditions. After every second tomography, the battery was translated out of the beam to collect open beam and dark field images to enable the correction and normalisation of the projections. For data processing the "Remove Outliers" and median filter of ImageJ Fiji[44] were used to remove white spots which are caused by fast neutrons and gamma radiation from the 16 bit images. Reconstruction of the tomographies was performed using the Octopus 8.9 software (XRE, Gent, Belgium) using the filtered back projection (FBP) reconstruction algorithm. Due to the high neutron absorption of lithium, the reconstructed slices were then corrected for beam hardening using the first tomogram to determine the parameters which are utilised for all following tomograms. The parameters are optimised in such a way that the lithium anode and the $SOCl_2$ cathode, in the middle of the cell, show a homogeneous attenuation coefficient respectively. Throughout the experiment 47 full tomograms were collected, 24 in forward and 23 in backward rotation with the process taking ca. 20.3 h and the battery providing a capacity of 506 mAh.

A second 4D neutron imaging scan with an 8 mA discharge current was performed on the IMAT neutron imaging beamline[45–47] at the ISIS neutron spallation source. In contrast to most reactor based neutron sources, neutron spallation sources such as the ISIS neutron source at the Rutherford Appleton Laboratory (UK) have a lower time-averaged neutron flux which makes imaging of dynamic processes with the conventional scanning strategies more difficult. To overcome this challenge, methods such as the Golden Ratio (GR) strategy can be employed. Using this method, the sample is imaged at non-regular intervals with the organisation of the angular distribution calculated by the GR. This method can be used for angular ranges of π or 2π with each consecutive scanning angle minimising the overlap of the previously scanned projections avoiding the acquisition of redundant information. GR projections are acquired continuously, over a chosen experimental period, enabling the optimisation of either the temporal or spatial resolution by post-image processing by selecting the number of projections from the GR tomogram that are reconstructed. By ensuring an overlap of the projections of consecutive tomographies in the projection sequence (i.e. taking a "running average") an improved time resolution is achieved. As the neutron flux at the ISIS spallation source is approximately 10× lower than at CONRAD-2 for the same L/D ratio, the GR decomposition strategy was applied here. An

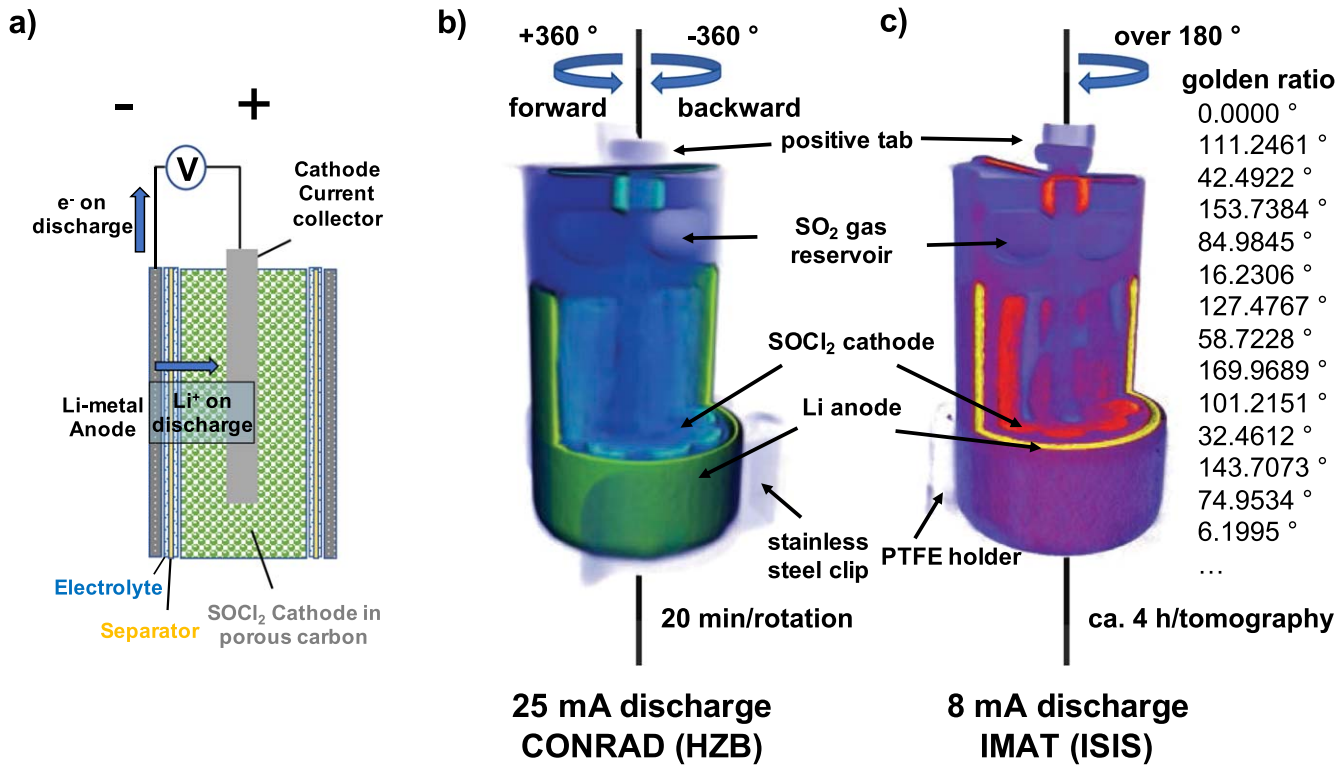

Figure 1. (a) Schematic illustration of a Li-metal/thionyl chloride bobbin type cell (b) 3D reconstruction of a LS 14250 cell discharged at 25 mA while being scanned on the CONRAD-2 neutron imaging beamline with sequences of equal angular projections in forward and backward rotation through 360° and (c) 3D reconstructions of a LS 14250 cell discharged at 8 mA scanned on the IMAT beamline with the GR decomposition strategy. The first projection angles for the GR scan are listed on the right hand side.

indirect detector box with a 80 μm thick ^{6}LiF/ZnS:Cu scintillator (Tritec, Switzerland) in combination with a Nikon photo lens (f = 135 mm, aperture 2) and an ANDOR Zyla sCMOS 4.2 PLUS camera (Oxford Instruments Andor, UK) was utilised. The box was adjusted to a pixel size of 29 μm with a pinhole size of 40 mm with a L/D ratio of ca. 250 which achieved a spatial resolution of about 80 μm. Once more, the plastic cover of the LS 14250 battery cell was removed, before the cell was inserted in a neutron transparent cylindrical PTFE sample holder. Electrical connections were maintained by attaching a copper cable between the negative battery can and the PTFE wall and attaching a crocodile clip to the positive battery tab. The PTFE holder was screwed to an adapter rod which was mounted onto a Huber Goniometer 411 (HUBER Diffraktionstechnik, Germany) rotation stage and positioned close to the camera box. Due to the limited rotation angle between 0° and 180° no specialised cable connection such as a slip ring was needed. Owing to the low neutron flux, a long exposure time of 30 s was used to maximise counting statistics. A GAMRY 1000E potentiostat discharged the cell at a constant current mode of 8 mA during the scan. The angular distribution for the whole scan was calculated using the GR with Fig. 1c showing a 3D reconstruction of the partially discharged cell and the first calculated GR projection angles over an angular range of π. In advance of the discharge scan of the cell, a 4 h tomography was acquired to enable a full reconstruction of the cell in pristine condition. After every 610 projections the cell was moved out of the beam for five open beam images to facilitate image correction after all the projections had been acquired. The total discharging process took about 104 h, after which the cell had delivered a capacity of 832 mAh. After correcting each projection using the dark and open beam images, and after filtering white spots, 3D reconstructions were performed via the FBP algorithm for a parallel beam using the ASTRA toolbox[48,49] reconstruction library within the python programming language. For the number of projections, the Fibonacci number 377 was utilised due to a better reconstruction result in combination with a shift of 188 projections for each following reconstruction. This results in an overlap of 189 projections and a time shift of about 2 h between the tomographies.

Four dimensional X-ray tomography was achieved on a Nikon XTH 225 laboratory X-ray system (Nikon Corporation, Japan) using a 225 kV reflection target source with a focal spot size of 3 μm at 7 W. A PerkinElmer 1620 16 bit (PerkinElmer Inc. USA) detector with a 2000 × 2000 pixel array and a pixel size of 200 μm was used to capture all images. The plastic cover of the cell was removed prior to mounting the cell with double-sided tape onto the sample holder of the rotation stage. An electrical connection was maintained by applying a crocodile clip to the positive tab, with the negative connection achieved by connecting a copper cable to the cell can using insulating tape. Both cables were then connected to an electrical slip ring (P4 + Compact Slip Ring, Moog, UK) which allowed a continuous rotation of the stage without losing the electrical connection. The battery was discharged using a GAMRY 1000E potentiostat (GAMRY Instruments, USA) in constant current mode with a discharge current of 25 mA. The instrument was programmed to continuously collect projections at an X-ray tube voltage level of 120 kV and current of 140 μA. To achieve one full tomogram, 1201 projections were captured through an angular range of 360° with an exposure time of 1 s per projection, leading to a total image acquisition time of ca. 20 min. The total cell discharge took about 18.3 h and reached a capacity of 459 mAh which enabled the capture of 56 full tomographies of the cell during discharge. The tomograms were reconstructed using the FDK (FDK_CUDA) circular cone beam reconstruction algorithm from the ASTRA toolbox[48,49] reconstruction library within the python programming language. Before starting the 3D reconstruction, the projections were corrected by the dark field and open beam images which were collected before and after the scan and binned by a factor of two to

reduce the reconstruction time and data size resulting in a reconstructed pixel size of 40.4 μm.

Results and Discussion

As shown in Fig. 2a the discharge curves of all three discharged LS 14250 cells show the typical flat discharge profiles at a high potential expected for the Li/$SOCl_2$ chemistry. The cells operated at the higher discharge current of 25 mA display a lower potential plateau at ca. 3.3 V with the cell discharged at 8 mA exhibiting a slightly higher potential plateau in excess of 3.4 V. At the beginning of the discharging process, the voltage delay, characteristic of Li/$SOCl_2$ cells, can be seen to be shorter for the cell discharged at a higher current requiring ca. 0.5 h before the potential is stabilised (Fig. 2c). In comparison, a long delay of about 30 h is observed for the low current discharge in Fig. 2a. This initial voltage delay occurs in Li/$SOCl_2$ cells due to the formation of a passivating LiCl layer at the anode during cell storage. The increased time needed to recover the normal potential of the cell observed during the low discharge is due to a reduced level of mechanical disruption, which removes the passivation layer on the lithium metal surface.[50] At the point the voltage recovers to a plateaued voltage the whole Li-metal surface can participate in the discharge reaction. The slightly lower potential of the cell scanned with X-ray compared to the one scanned with neutrons is attributed to manufacturing variations. The difference in cell capacity of 459 mAh compared to 506 mAh may be a result of a higher self-discharge during a longer cell storage time, or differences in the active mass loading during manufacture. Internal mechanisms in the cell such as the shielding of active electrode material by a SO_2 gas layer on the Li-metal surface can result in similar effects.

Laboratory X-ray scanners or synchrotron imaging beamlines in the intermediate or lower hard X-ray energy regime show lithium metal or lithium diffusion in a lithium battery cell only indirectly by a grey value increase in the electrode, where the lithium is removed and a grey value reduction where lithium is deposited. This behaviour is visible for the LS 14250 cell scanned with X-rays in Fig. 3, which shows horizontal and vertical slices of the pristine, half discharged and fully discharged cell. The metallic battery components such as the positive tab, the negative cell can and the cathode current collector are clearly visible, with the battery header somewhat obscured due to reconstruction artefacts. Furthermore, the liquid $SOCl_2$ cathode in the middle of the cell can be seen; however, the $SOCl_2$:$LiAlCl_4$ electrolyte is not distinguishable from the liquid cathode. Regions which are filled with an excess of electrolyte are expected in this cell type and can be seen above the active cell material by a reduction of the electrolyte volume and an increase of the gas volume in the battery head during the discharge. The lithium metal anode is indirectly visible by the transparent region at the outer cell radius between cathode and the stainless steel cell can. The removal of lithium from the electrode is indirectly detected during the discharge process. A contrast change inside the $SOCl_2$ cathode is not detected. During the discharging process SO_2 gas is formed from the reaction of lithium with $SOCl_2$ which is visible as bright purple areas due to a low attenuation coefficient, which is similar to air. Shortly after the initiation of the discharge process, the SO_2 gas forms bubbles in the cathode which diffuse into four gas channels, which work as gas guides in the porous carbon mesh, and accumulate inside the cell header where a further gas reservoir is located. This transfer of SO_2 gas away from the cathode is designed to prevent the stagnation of lithium diffusion and subsequent passivation of the anode surface during the discharge. A distinction between the evolved SO_2 gas and the lithium metal is not possible in the X-ray image, because the greyscale values cannot be sufficiently differentiated.

To provide a better understanding of the processes involved in the discharge of the cell, including the removal of Li from the metal anode and the diffusion process inside the $SOCl_2$ cathode, complementary neutron imaging was used. Time resolved neutron tomography mitigates the challenges associated with X-ray imaging discussed previously, and due to the high sensitivity of neutrons to lithium, a quantitative description of the Li removal from the anode and the diffusion of Li inside the thionyl chloride cathode can be achieved. Figure 4 shows orthogonal slices obtained on CONRAD-2 from the cell discharged at 25 mA: in pristine condition, halfway through discharge and fully discharged, at which point the cell had delivered a capacity of 506 mAh. In contrast to the X-ray tomographies, neutrons exhibit just a weak attenuation by the metallic cell components such as the stainless steel container or the positive battery tab. As seen in Fig. 4, the Ni, cathode current collector exhibits a similar neutron attenuation to the surrounding liquid $SOCl_2$ cathode and is difficult to distinguish. However, as the Li content in the cathode increases, the current collector becomes more visible. More highly attenuating cell components, such as the boron containing glass seal which shields the environment from the toxic SO_2 gas and the Li, are shown in bright yellow colours. As previously shown in the X-ray images (Fig. 3), a contrast difference between the electrolyte and the liquid cathode in the pristine state is not observed, however, as the discharge process progresses the

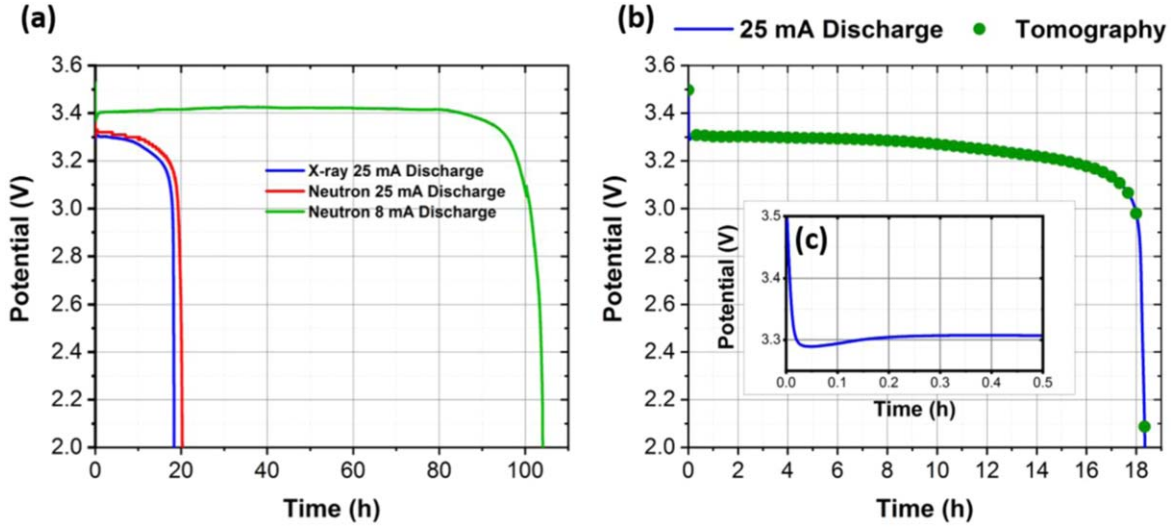

Figure 2. (a) Discharge curves of the three LS 14250 cells used in this work, two discharged at 25 mA scanned with X-rays and neutrons and one cell at 8 mA imaged with neutrons (b) A detailed discharge curve of the cell discharged at 25 mA scanned with X-rays. Green dots mark the times when tomograms were recorded. (c) a magnified view of the voltage delay at the beginning of the cell discharging process, typical for Li/$SOCl_2$ chemistry.

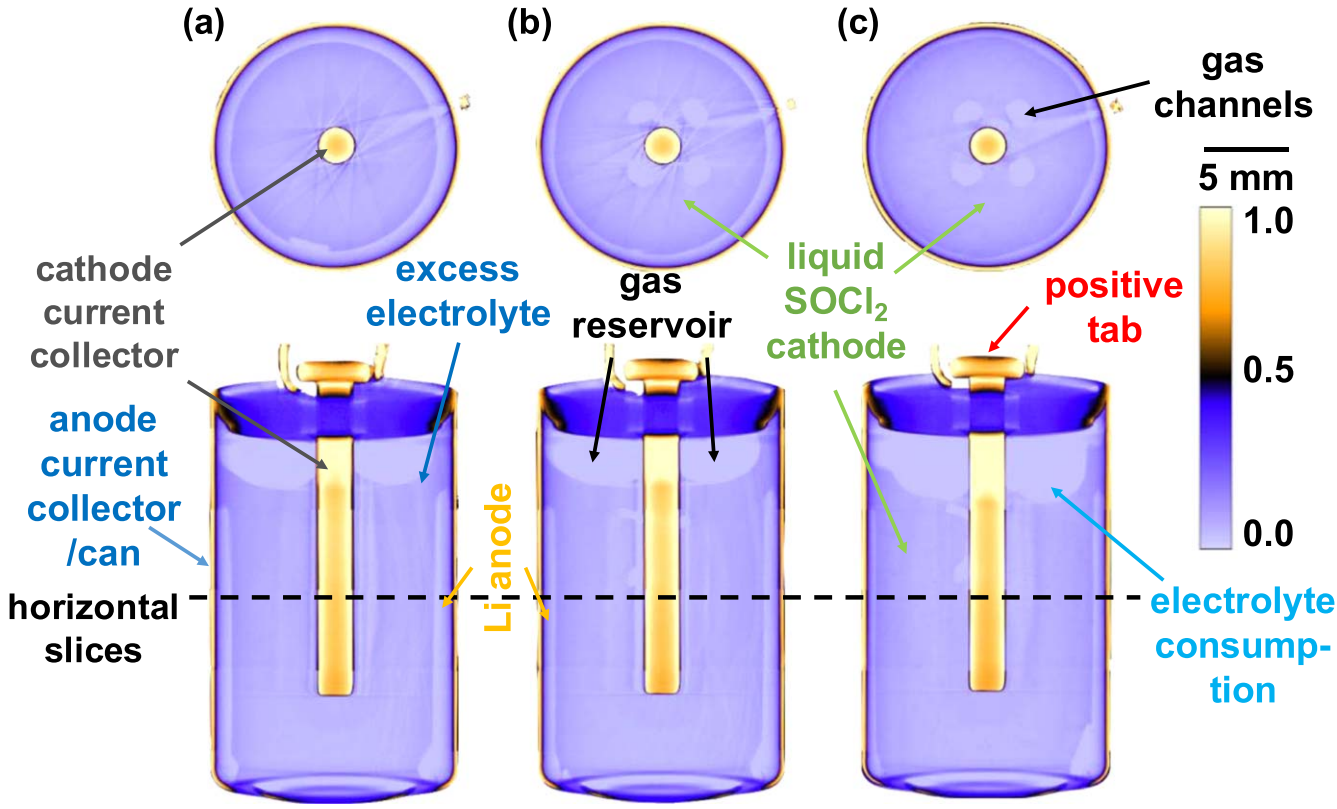

Figure 3. Orthogonal slices from the 4D X-ray scan of the LS 14250 battery cell discharged at 25 mA, showing horizontal and vertical orthogonal slices from the in operando X-ray scan at three different SoCs; pristine, half discharged and the fully discharged cell.

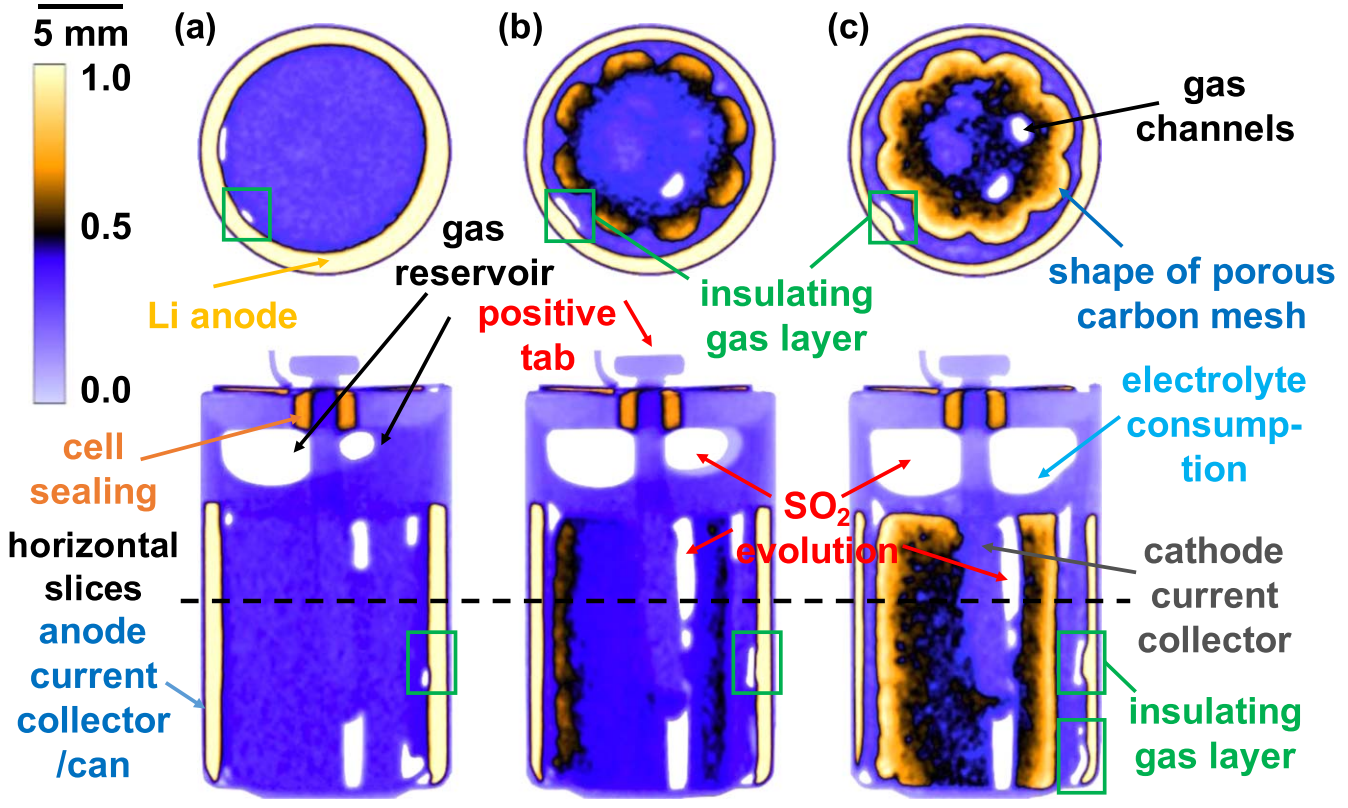

Figure 4. Orthogonal slices from the in-operando 3D neutron experiment of the LS 14250 cell discharged at 25 mA at the CONRAD-2 neutron imaging beamline at three different SoCs: pristine, half discharged and fully discharged cell.

cathode can be clearly distinguished from the electrolyte due to the increase of the attenuation coefficient indicated by the colour change from purple to black to yellow. The volume reduction in the excess electrolyte in the battery header becomes visible as the discharge progresses, exposing the "flower" like shapes of the supporting porous carbon skeleton alongside the four gas channels in the horizontal orthoslices. During the discharge process, Li is progressively removed from the metal anode around the cathode and diffuses through the separator membrane, (which is not visible due to insufficient spatial resolution), into the cathode. Here, the attenuation coefficient increases steadily, seen by an increase in contrast starting from the cathode border. As more Li moves into the cathode a high contrast gradient from the cathode edge into the middle of the cell can be seen. This is indicative of a slow lithium diffusion rate inside the cathode. At the same time, SO_2 gas, which is neutron transparent, evolved through the discharge reaction and is marked through an increase of lowly attenuating regions in Fig. 4. Towards the edge of the cathode, a larger volume of gas is generated due to the higher Li concentration in close proximity to the anode and consequent increased reactivity in this region. Not all of this gas diffuses into the gas channels and fills the gas reservoir, with a portion diffusing through the electrolyte and, in places, covering the surface of the anode, highlighted by green boxes in the slices in Fig. 4. Such "gas shielded" Li surface areas cannot participate in the chemical reaction. As a result of the slow lithium mobility in the cathode and the shielding of fresh lithium from the anode by gas the cell performance is inhibited through a reduction in both the cell capacity and operating potential.

The second neutron imaging experiment provided data on a similar LS 14250 cell which was discharged at a lower discharge current of 8 mA. Orthogonal slices of three tomographies from IMAT are displayed in Fig. 5, with slices from the pristine cell, in a half discharged condition and the fully discharged state with the cell yielding a total capacity of 832 mAh. The cell shows a similar discharge behaviour to that discharged at 25 mA, however, due to the lower discharge current the cell provided a ca. 40% increase in capacity. This resulted in an increase in the consumption of lithium as seen in Fig. 5, with the inhomogeneity of the lithium removal throughout the cell being particularly notable. The horizontal slices in Fig. 5 initially show a homogeneous Li-metal anode in the pristine state and with the highly attenuating layer being preferentially removed towards the lower half and right hand side of the cell during discharge. This inhomogeneous Li consumption is likely caused by a misalignment of the cathode which is seen to be closer to the lower right anode side providing a shorter path to the cathode. Furthermore, evidence of the ability for gas to diffuse in this right hand region is shown in the tomograms with an area of gas evident at the surface of the anode observed when the cell is half-discharged not being present on full discharge. The lower discharge current used here also influences the quantity and depth of diffusion of Li in the cathode, which increases at lower operating currents due to the slow Li diffusion process in $SOCl_2$. This increased Li diffusion inside the cathode is likely the key reason for the improved cell capacity observed in this instance. At higher discharge currents, an increasing amount of lithium reacts in the outer cathode region, forming insulating solid sulphur, which is deposited in the channels of the porous carbon skeleton blocking the gas diffusion channels and ultimately insulating the internal cathode where fresh $SOCl_2$ is available, thereby reducing the cell capacity.

By taking advantage of the high sensitivity of neutrons to Li shown previously, a quantitative determination of the Li-anode volume over the discharge time is possible. Here, a constant threshold segmentation of the bright lithium anode was achieved by using the AVIZO visualisation software suite (Thermo Fisher Scientific, USA) with the results shown alongside the discharge curves in Fig. 6. In the case of the battery cell discharged at 25 mA, the 24 tomographies measured in the forward rotation direction were used for the segmentation. Three of the segmented volumes are visualised in Fig. 6b. In the pristine state a total Li volume of 615 mm^3 was measured with 356 mm^3 remaining after the discharge

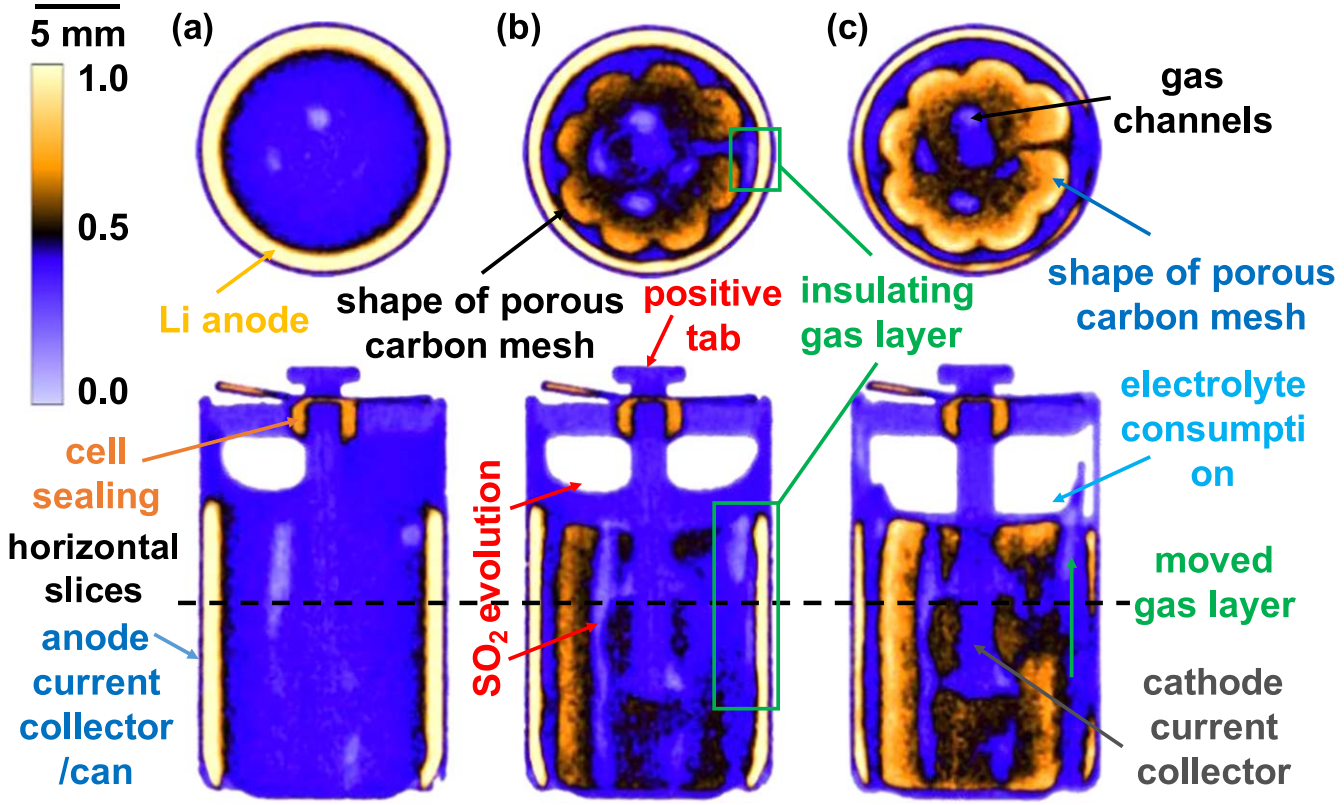

Figure 5. Orthogonal slices from the in-operando 3D neutron experiment of the LS 14250 cell discharged at 8 mA at the IMAT neutron imaging beamline at three different SoCs; pristine, half discharged and fully discharged cell.

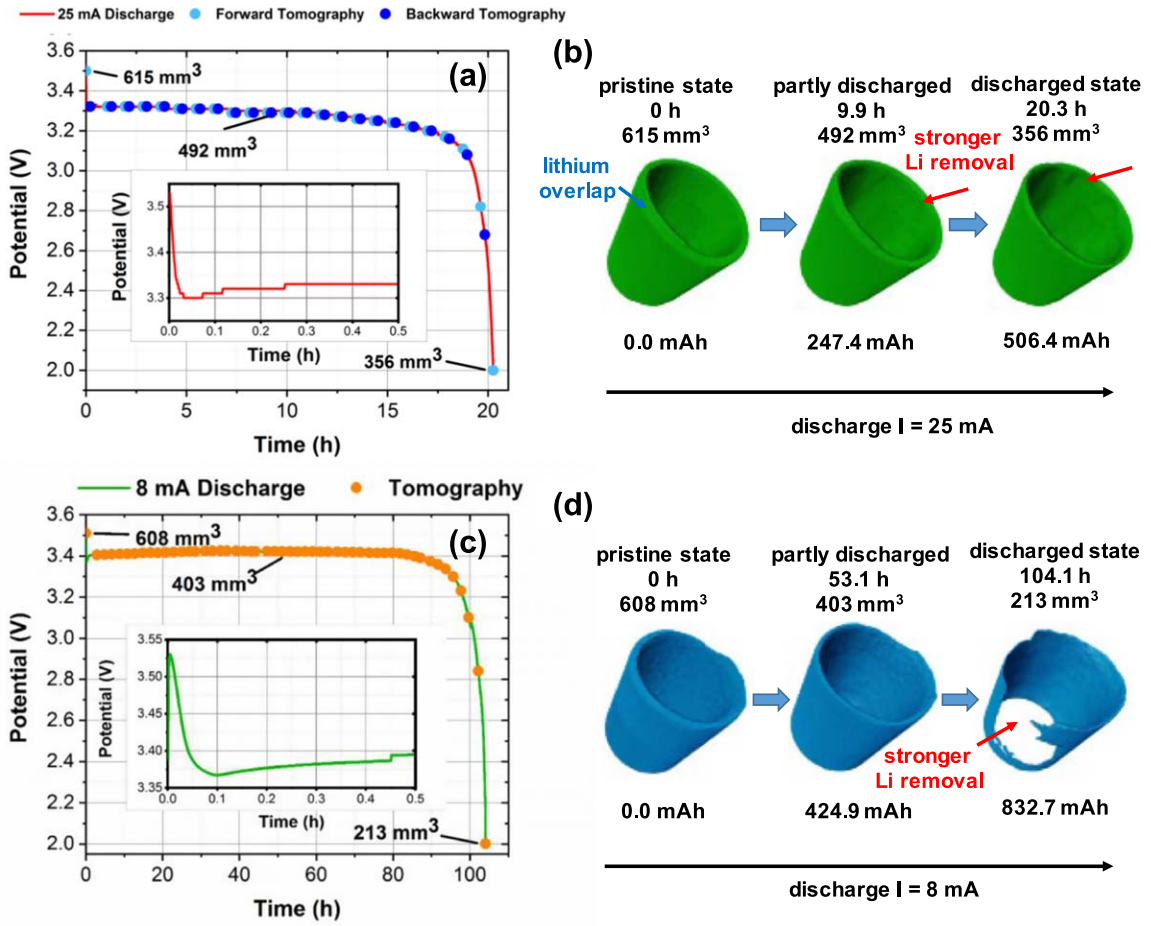

Figure 6. Discharge curve of the LS 14250 cell discharged at (a) 25 mA and (c) 8 mA alongside volume renderings of the anode volumes of the cells discharged at (b) 25 mA and (d) 8 mA at different SoCs with the pristine, half and fully discharged state.

process was complete. The anode shows a flat and homogeneous inner and outer surface area in the pristine state. During the discharge process progressive lithium removal is clearly visible at the internal electrode in the shape of vertical stripes. These stripes are located directly opposite the bulges of the "flower" shaped cathode seen in Figs. 4 and 5. The shorter distance between the electrodes at these locations facilitates increased Li removal from the anode. The overlap of the Li-metal at the left side of the segmented anode, caused by the manufacturing process, is also visible with a shift in height between both endings.

While the initial Li volume of the cell discharged at 8 mA is similar (608 mm^3) the Li volume change is more substantial, with 213 mm^3 remaining in the fully discharged state. Here, the Li anode volume was determined for every second tomography. No overlap of the lithium metal foil endings is visible which may be a result either of better initial fabrication or insufficient spatial resolution. During the discharge process more lithium is consumed owing to the lower discharge current, resulting in the complete removal of Li at one side of the anode.

Quantification of this Li volume decrease is achieved by correlating the volume of Li at a given time to the capacity provided by the cell with this relationship following a linear trend as observed in Fig. 7. The initial Li metal volumes of 615 mm^3 and 608 mm^3, which correspond to a Li mass of ca. 0.32 g per cell (based on a Li density at 20 °C of 0.534 g cm^{-3}), are in a good agreement with the manufacturer's data sheet values of approximately 0.3 g per cell. The theoretical relationship between the used Li volume in mm^3 and the resulting capacity delivered in Ah is given in Eq. 3. Here, M_{Li} corresponds to the molar mass of lithium, C the electric charge, N_A the Avogadro constant and ρ_{Li} the density of lithium.

$$\left[\frac{mm^3}{Ah}\right] = \frac{M_{Li} \cdot 3600\left[\frac{s}{h}\right]}{C \cdot N_A \cdot \rho_{Li}} = 485\frac{mm^3}{Ah} \quad [3]$$

It can be seen that a Li removal rate of 485 mm^3 Ah^{-1} is theoretically required for a Li/$SOCl_2$ cell which corresponds to a minimum initial Li volume of 582 mm^3, or mass of 0.31 g, for the cells examined in this work. By comparing this to the measured volumes it can be seen that in this case the significant majority of the anode must be consumed to deliver the rated 1.2 Ah capacity. Experimentally determined Li removal rates can be calculated by interrogating the slope of the curves shown in Fig. 7. Here it is shown that 514 mm^3 Ah^{-1} and 462 mm^3 Ah^{-1} are required for the cells discharged at 25 and 8 mA, respectively. The discrepancy between the values for the two cells can be explained by different thresholds for the volume segmentation arising from the different neutron spectra of CONRAD-2 and IMAT which result in different average attenuation coefficients for Li. Further, a slightly different utilised threshold can affect a deviation of several cubic millimetres as well as the relative big pixel sizes which can lead to a slightly higher or lower determined lithium volume. To provide a more representative comparison with this theoretical value it is beneficial to use the mean of 488 mm^3 Ah^{-1} of the two measured values.

A considerable drawback of the $SOCl_2$ electrode chemistry is the slow Li diffusion inside the cathode which can result in blocking of the diffusion channels in the carbon support skeleton by the formation of solid sulphur from the chemical reaction with lithium. Quantification of this can be achieved by examining changes in intensity, which indicates the Li diffusion throughout the cell.

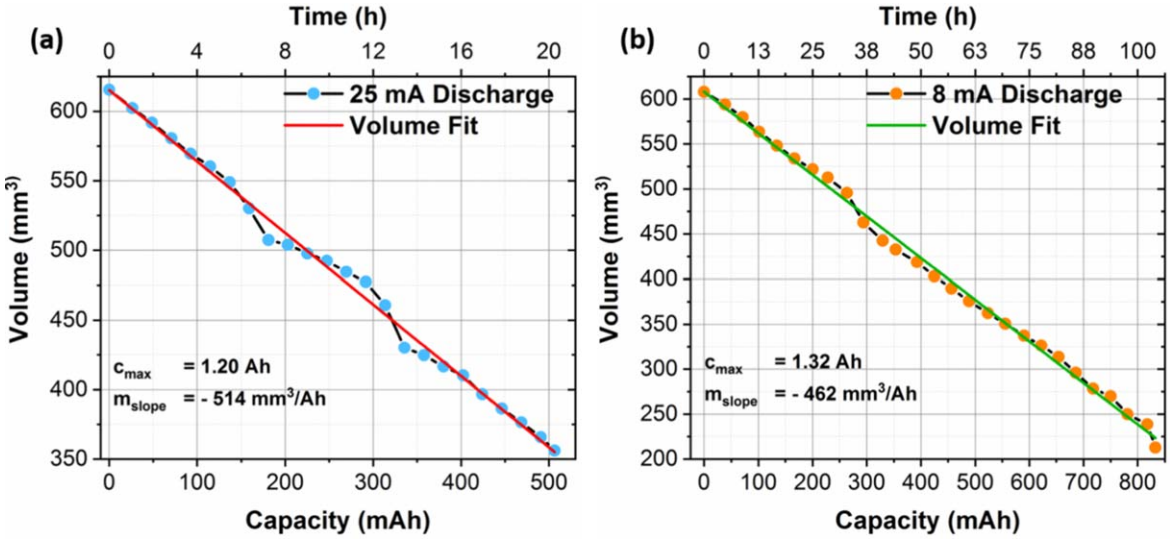

Figure 7. Lithium volume decrease of the LS 14250 anode during a discharge current of (a) 25 mA and (b) 8 mA, respectively. The deviations from the expected linear volume reduction are due to variations in the segmentation process. The total error of the lithium volume determination is estimated to be smaller than 5%.

Figures 8c, 8d shows profiles of the intensity through the reconstructed slices of the anode and cathode for both the cell discharged at 25 mA and 8 mA. For the line profiles a single horizontal orthogonal slice was used, which is the most representative for the battery cell respectively, shown in Figs. 8a, 8b. A high lithium mobility can be seen at the cathode edges over the discharge time for both cells, with the 25 mA discharged cell showing a higher mobility as a result of the increased discharge current (Figs. 8c, 8d).

The *x*-axis shows the radial distance from the centre of the cell, and the *y*-axis the relative change of the lithium distribution in terms of greyscale values normalised to the initial SoC. Values above the baseline are attributable to an increased lithium content (such as that observed in the $SOCl_2$ electrode), with reductions in intensity associated with a decrease of lithium concentration (as seen in the lithium metal anode). The low lithium amount in the inner cathode region, shown by a trough in intensity towards the centre of the cell indicates a substantial stagnation in the lithium diffusion at a 25 mA discharge current. Figure 8a shows related horizontal slices where blue and red colours indicate the lithium removal and deposition, respectively. A high lithium accumulation at the bulges of the "flower" shaped cathode boundary is clearly visible during the first discharge phase due to the favourable short distance between the lithium metal anode and the cathode. At the end of the discharging process, the red ring along the cathode border indicates high accumulation of lithium in contrast to the inner cathode region which is almost devoid of lithium. It should be noted that the blue coloured, circular regions inside the cathode are related to intensity changes in the reconstructions caused by the generation of SO_2 gas which fill the gas channels, displacing the $SOCl_2$ and causing a similar behaviour to that observed during Li removal from the anode. White areas represent no intensity changes during the discharging process which indicates regions with constant lithium amounts or regions unaffected by the reaction.

Figures 8b, 8d shows a similar analysis for the cell discharged at 8 mA. In this case, the line profile plot shows a more equal Li distribution from the outer cathode edge to the centre of the cell. The lower discharge current facilitates improved Li diffusion properties due to the reduced reaction rate. The improved ratio can be seen by the higher lithium amount in the centre of the cathode in comparison to the cell discharged at 25 mA. The horizontal slices in Fig. 8b also show a more homogeneous lithium distribution during the discharge before the concentration increases on the cathode border due to blocking effects in the carbon skeleton. This comparison of the time dependent lithium distributions inside the $SOCl_2$ electrode reveals the major reason for the capacity loss with discharge at higher currents. The loss of usable cell capacity is strongly correlated to the rate of the lithium diffusion inside the cathode. Higher currents force the chemical reaction between the Li and the thionyl chloride whereby solid sulphur is formed impeding the diffusion channels of the porous supporting carbon skeleton and reducing the rate of Li diffusion. As a consequence, fresh unreacted $SOCl_2$, stored in the inner cathode region, cannot participate in the reaction.

To better understand the problem of capacity loss at higher discharge rates, an improved understanding of the lithium diffusion process in the cathode is necessary with results detailed in Fig. 9 in which the time dependent normalised intensity change at seven different positions, starting at the cathode edge and evenly distributed regions along the arrow towards the centre, is measured in the most representative horizontal slices for both discharge rates. The detected normalised intensity can be interpreted as a measure of the quantity of Li present at any given position. Figure 9a presents the normalised intensity change from a radial distance of −5.0 to 0.0 mm for the cell discharged at 25 mA. The values were determined along a representative line which is shown in the orthoslice at different distances from the cathode centre. The line was placed in such a way that the gas channels do not influence the measurement result. The results shown in Fig. 9a indicate an increased level of lithium at a radius of −5.0 mm, which steadily decreases through the cell to a boundary located at a radius of ca. −2.5 mm, beyond which no lithium is seen to diffuse. Above approximately 350 mAh, the lithium diffusion at the outer cathode part can be seen to plateau, indicating a saturation of the cathode. However, due to the constant current discharge this stagnation of the Li diffusion must be compensated by an increased rate of Li diffusion elsewhere. It is likely that this happens in the gaps between the "flowery" bulges at the cathode boundary, which are more active than other regions during the initial part of discharge process owing to the shorter diffusion paths for the Li-ions from anode to cathode. The rate of Li diffusion seems to only stagnate in the outer cathode region (−5.0 mm) with an increase in intensity, and consequently continued diffusion, evident in the inner regions (−4.2 mm to −2.5 mm) suggesting that the limitation on the capacity provided by the cell occurs in the outer cathode shell area.

At a lower discharge current, the lithium diffusion inside the cathode is slightly more homogeneous with a noticeable decrease inwards the cathode. Figure 9b shows the lithium diffusion behaviour inside the $SOCl_2$ cathode for the cell discharged at 8 mA. In contrast to the higher discharge current of 25 mA, the rate of intensity rise is consistent across all regions, with the internal regions displaying a substantially increased change in intensity.

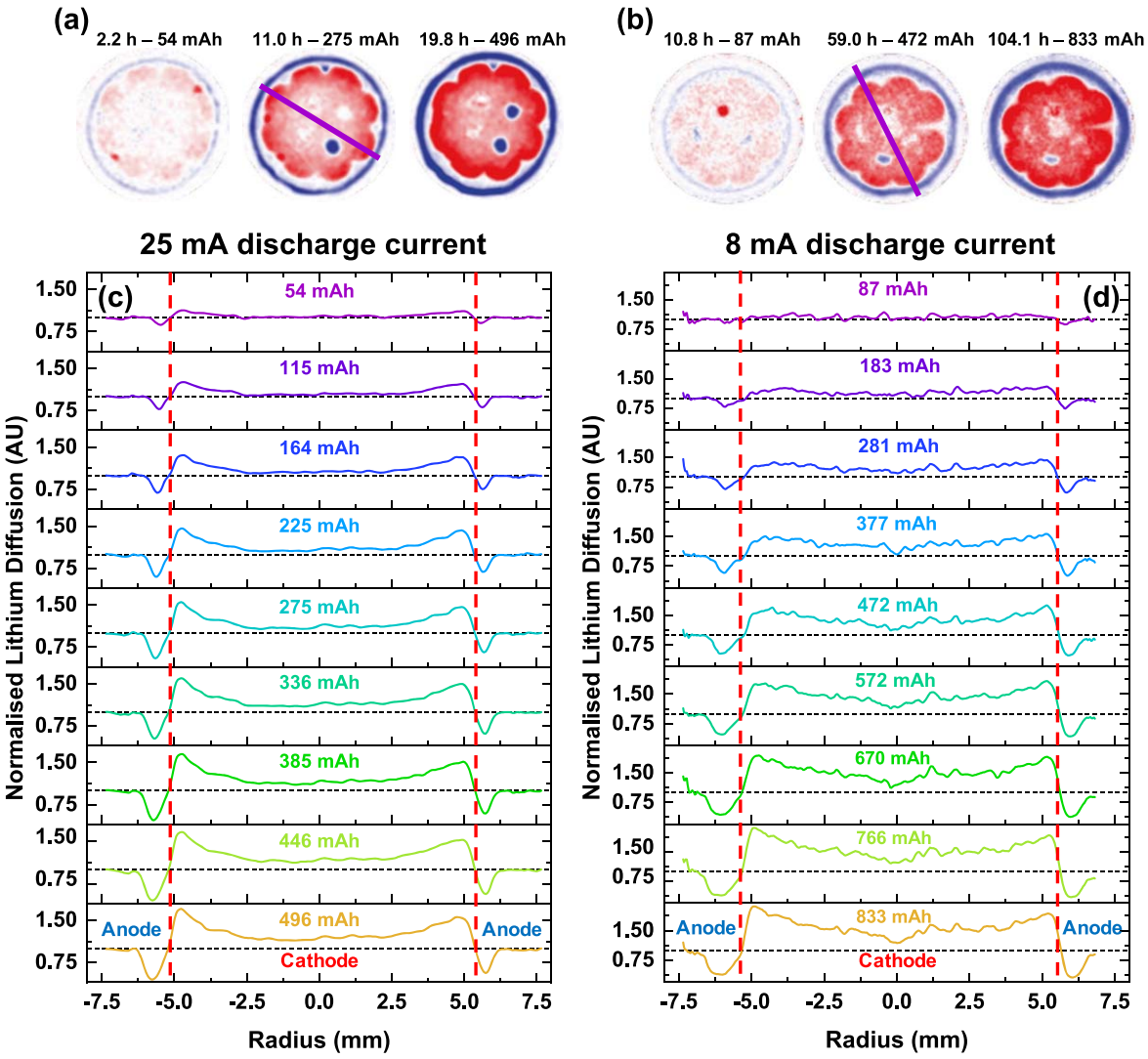

Figure 8. Normalised grey values representing lithium redistributions inside the LS 14250 battery cell during a discharge current of – (a), (c) 25 mA and (b), (d) 8 mA. (a), (b) selected horizontal slices from the middle part of the cell at different SoCs highlighting lithium removal and accumulation. (c), (d) time dependent line plots through the middle section of a LS 14250 Li/$SOCl_2$ cell during the discharging process. Values above the baseline indicate an increase of lithium in the cathode, and values below the baseline indicate lithium removal from the anode.

These findings demonstrate the mechanisms behind the improved capacity provided by lower operating currents, which enables Li diffusion deeper inside the cathode enabling use of more unreacted $SOCl_2$.

The spatially variant intensity increase per capacity is a useful metric to compare the Li diffusion behaviour inside the cathode for different discharge currents. The intensity-capacity slopes for the graphs plotted in Fig. 9 are displayed over the cathode radial distance in Fig. 10. The slope values over the radial distance show a linear decrease of Li diffusion, with an increased rate observed for the cell discharged at 25 mA scan due to higher Li use. At a radius of about −1.5 mm the lithium diffusion seems to stop while the cell discharged at 8 mA shows evidence of Li diffusion throughout the entire cell. The point shown at 0.0 mm includes a small contribution in intensity of the cathode current collector which causes a slightly elevated change. A fit of the slope of the linear region is a measure of the capacity and radius dependent Li diffusion which is −0.379 (Int Ah^{-1}) mm^{-1} for the cell discharged at 25 mA and −0.083 (Int Ah^{-1}) mm^{-1} for that at 8 mA. From the slope it is possible to determine a maximum discharge current which enables the full capacity to be utilised. The Li diffusion per capacity and radius is plotted over the discharge current in Fig. 10b. Assuming a linear dependence for both values, the abscissa-axis intersection represents the maximal discharge current to reach the full cell capacity and is marked with a green dot which corresponds to approximately 3.2 mA. This maximum cell utilisation rate is an order of magnitude lower than the maximum recommended continuous current of 35 mA and demonstrates the capacity limitation encountered at maximum discharge rate.

Conclusions

Multi-modal tomography was performed using X-rays and neutrons to elucidate the dynamic processes which occur inside primary $LiSOCl_2$ cells during discharge. These complementary methods enable the visualisation of the changes which occur in the cell components due to the different attenuation characteristics in the two techniques. X-ray tomography identified the consumption of the $SOCl_2$ electrolyte, which resulted in the evolution of SO_2 gas; however no significant structural deformations were observed using this method. In contrast, neutron imaging enabled the identification of the rate dependent diffusion characteristics of Li within the cell. Time dependent neutron tomography was enabled through the use of the golden ratio imaging technique, which substantially improves the temporal resolution of the imaging process, even at low flux neutron sources. The gas evolved during discharge was found to inhibit the performance by isolating

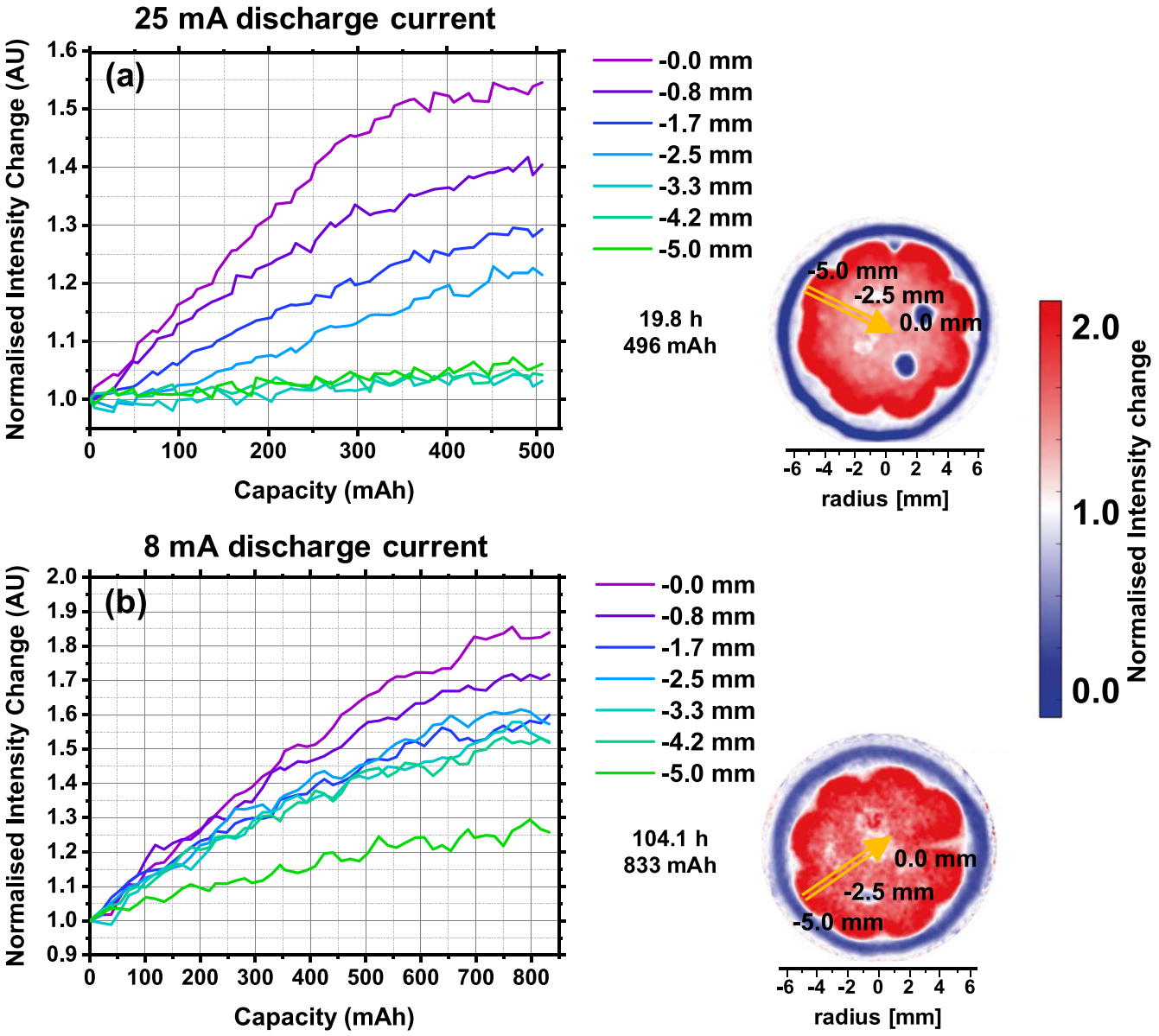

Figure 9. Relative grey value changes representing lithium diffusion inside the $SOCl_2$ cathode at (a) 25 mA and (b) 8 mA alongside horizontal slices from the middle of the cell, with the yellow arrow pointing along the selected analysis points.

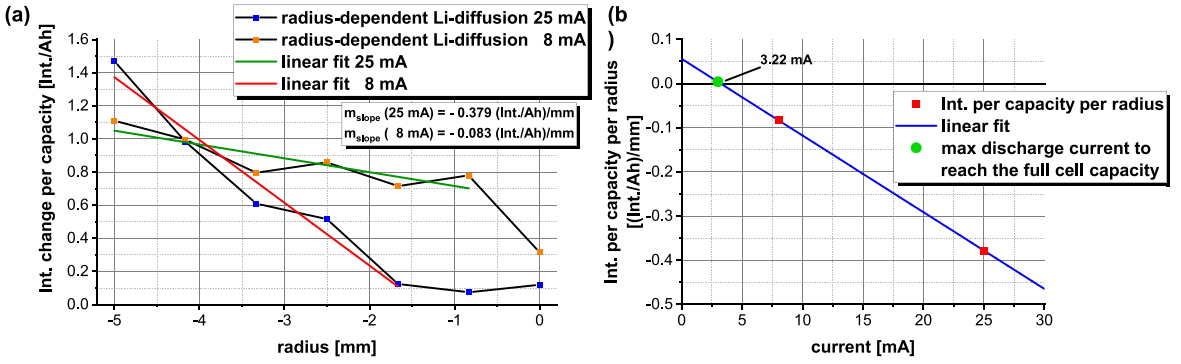

Figure 10. Determination of the intensity/lithium amount change per cell capacity and the maximal discharge current which allows for the use of the full cell capacity showing (a) the observed intensity change, and the calculated slopes for the cells discharged at 25 mA and 8 mA and (b) an estimation of the maximal usable discharge current to reach the full cell capacity occurring at the intersection of the curve with the abscissa.

regions of Li. Furthermore, the rate of Li diffusion was observed to be spatially variable, with regions identified where the diffusion process was seen to stagnate during discharge.

The two imaging methods have provided an improved understanding of the performance of the cells. Where X-rays are more sensitive to metallic cell components such as the battery casing or the current collectors, neutrons visualise inter alia the lithium diffusion. The combination of both techniques helps to understand processes which are hidden for one technique or localise battery components, such as the cathode current collector in the cell centre, which are invisible for neutrons but the location is important for the analysis. For the discharge currents used in this study, the capacity of the cells was observed to fall significantly short of the nominal capacity, due to the slow lithium diffusion and the presence of unusable lithium. This bobbin type cell design shows significant radial disparity in the rate of Li diffusion at higher discharge rates suggesting a need to either limit the maximum current drawn from the cell or amend the cell design to promote improved Li diffusion. A calculation to determine the maximum capacity with this cell design suggests that the discharge rate (to ensure maximum capacity) should be at least an order of magnitude lower than the maximum current suggested by the manufacturer.

Acknowledgments

This work was carried out with funding from the Faraday Institution (faraday.ac.uk; EP/S003053/1FIRG003, FIRG013, FIRG014). We would like to acknowledge the EPSRC (ER/M028100/1) and The Royal Academy of Engineering (CiET1718/59) for financial support. Measurements were carried out at the CONRAD-2/ V7 instrument at Helmholtz-Zentrum Berlin (HZB). We thank HZB for the allocation of neutron radiation beamtime. The provision of neutron beamtime on IMAT at ISIS (RB181068: DOI: 10.5286/ISIS.E.95665718) is gratefully acknowledged.

ORCID

Ralf F. Ziesche https://orcid.org/0000-0001-7955-6893
James B. Robinson https://orcid.org/0000-0002-6509-7769
Matthew D. R. Kok https://orcid.org/0000-0001-8410-9748
Henning Markötter https://orcid.org/0000-0003-3464-6793
Winfried Kockelmann https://orcid.org/0000-0003-2325-5076
Nikolay Kardjilov https://orcid.org/0000-0002-0980-1440
Ingo Manke https://orcid.org/0000-0001-9795-5345
Dan J. L. Brett https://orcid.org/0000-0002-8545-3126
Paul R. Shearing https://orcid.org/0000-0002-1387-9531

References

1. D. C. Bock, A. C. Marschilok, K. J. Takeuchi, and E. S. Takeuchi, "Batteries used to power implantable biomedical devices." *Electrochim. Acta*, **84**, 155 (2012).
2. W. Chen, J. Liang, Z. Yang, and G. Li, "A review of lithium-ion battery for electric vehicle applications and beyond." *Energy Procedia*, **158**, 4363 (2019).
3. Y. Borthomieu, *Satellite Lithium-Ion Batteries* (Elsevier, Amsterdam) (2014).
4. R. Gangadharan, C. Electrochemical, P. N. N. Namboodiri, K. V. Prasad, and R. Viswanathan, "The lithium-thionyl chloride battery—a review." *J. Power Sources*, **4**, 1 (1979).
5. A. J. Hills and N. A. Hampson, "The $LiSOCl_2$ cell—a review." *J. Power Sources*, **24**, 253 (1988).
6. J. J. Auborn, K. W. French, S. I. Lieberman, V. K. Shah, and A. Heller, "Lithium anode cells operating at room temperature in inorganic electrolytic solutions." *J. Electrochem. Soc.*, **120**, 1613 (1973).
7. W. K. Behl, J. A. Christopulos, M. Ramirez, and S. Gilman, "Lithium inorganic electrolyte cells utilizing solvent reduction." *J. Electrochem. Soc.*, **120**, 1619 (1973).
8. M. Babai and M. Pallivathikal, "Comparison of the behavior of the Li/$SOCl_2$ and Ca/$SOCl_2$ systems at elevated temperatures." *J. Power Sources*, **28**, 325 (1989).
9. C. R. Schlaikjer, F. Goebel, and N. Marincic, "Discharge reaction mechanisms in Li / SOCl2 cells." *J. Electrochem. Soc.*, **126**, 513 (1979).
10. P. R. Shearing, N. P. Brandon, J. Gelb, R. Bradley, P. J. Withers, A. J. Marquis, S. Cooper, and S. J. Harris, "Multi length scale microstructural investigations of a commercially available Li-Ion battery electrode." *J. Electrochem. Soc.*, **159**, A1023 (2012).
11. D. P. Finegan et al., "Characterising thermal runaway within lithium-ion cells by inducing and monitoring internal short circuits." *Energy Environ. Sci.*, **10**, 1377 (2017).
12. D. P. Finegan, B. Tjaden, T. M. M. Heenan, R. Jervis, M. Di Michiel, A. Rack, G. Hinds, D. J. L. Brett, and P. R. Shearing, "Tracking internal temperature and structural dynamics during nail penetration of lithium-ion cells." *J. Electrochem. Soc.*, **164**, A3285 (2017).
13. D. P. Finegan et al., "In-operando high-speed tomography of lithium-ion batteries during thermal runaway." *Nat. Commun.*, **6**, 1 (2015).
14. D. P. Finegan, M. Scheel, J. B. Robinson, B. Tjaden, M. Di Michiel, G. Hinds, D. J. L. Brett, and P. R. Shearing, "Investigating lithium-ion battery materials during overcharge-induced thermal runaway: an operando and multi-scale X-ray CT study." *Phys. Chem. Chem. Phys.*, **18**, 30912 (2016).
15. D. P. Finegan et al., "Quantifying bulk electrode strain and material displacement within lithium batteries via high-speed operando tomography and digital volume correlation." *Adv. Sci.*, **3**, 1500332 (2016).
16. L. Zielke, T. Hutzenlaub, D. R. Wheeler, I. Manke, T. Arlt, N. Paust, R. Zengerle, and S. Thiele, "A combination of X-ray tomography and carbon binder modeling: reconstructing the three phases of LiCoO2 Li-ion battery cathodes." *Adv. Energy Mater.*, **4**, 2 (2014).
17. A. G. Kashkooli, S. Farhad, D. U. Lee, K. Feng, S. Litster, S. K. Babu, L. Zhu, and Z. Chen, "Multiscale modeling of lithium-ion battery electrodes based on nano-scale X-ray computed tomography." *J. Power Sources*, **307**, 496 (2016).
18. S. R. Daemi, C. Tan, T. Volkenandt, S. J. Cooper, A. Palacios-Padros, J. Cookson, D. J. L. Brett, and P. R. Shearing, "Visualizing the carbon binder phase of battery electrodes in three dimensions." *ACS Appl. Energy Mater.*, **1**, 3702 (2018).
19. P. Boillat, E. H. Lehmann, P. Trtik, and M. Cochet, "Neutron imaging of fuel cells —recent trends and future prospects." *Curr. Opin. Electrochem.*, **5**, 3 (2017).
20. P. Oberholzer and P. Boillat, "Local characterization of PEFCs by differential cells: systematic variations of current and asymmetric relative humidity." *J. Electrochem. Soc.*, **161**, F139 (2014).
21. Y. Wu et al., "Investigation of water generation and accumulation in polymer electrolyte fuel cells using hydro-electrochemical impedance imaging." *J. Power Sources*, **414**, 272 (2019).
22. M. Maier et al., "Mass transport in polymer electrolyte membrane water electrolyser liquid-gas diffusion layers: a combined neutron imaging and X-ray computed tomography study." *J. Power Sources*, **455** (2020).
23. C. H. Lee et al., "The effect of cathode nitrogen purging on cell performance and in operando neutron imaging of a polymer electrolyte membrane electrolyzer." *Electrochim. Acta*, **279**, 91 (2018).
24. J. B. Siegel, X. Lin, A. G. Stefanopoulou, D. S. Hussey, D. L. Jacobson, and D. Gorsich, "Neutron imaging of lithium concentration in lfp pouch cell battery." *J. Electrochem. Soc.*, **158**, A523 (2011).
25. J. B. Siegel, A. G. Stefanopoulou, P. Hagans, Y. Ding, and D. Gorsich, "Expansion of lithium ion pouch cell batteries: observations from neutron imaging." *J. Electrochem. Soc.*, **160**, A1031 (2013).
26. H. Zhou, K. An, S. Allu, S. Pannala, J. Li, H. Z. Bilheux, S. K. Martha, and J. Nanda, "Probing multiscale transport and inhomogeneity in a lithium-ion pouch cell using in situ neutron methods." *ACS Energy Lett.*, **1**, 981 (2016).
27. G. V. Riley, D. S. Hussey, and D. L. Jacobson, "In situ neutron imaging of alkaline and lithium-ion batteries." *ECS Trans.*, **25**, 75 (2010).
28. M. Lanz, E. Lehmann, R. Imhof, I. Exnar, and P. Novák, "In situ neutron radiography of lithium-ion batteries during charge/discharge cycling." *J. Power Sources*, **101**, 177 (2001).
29. B. Michalak, H. Sommer, D. Mannes, A. Kaestner, T. Brezesinski, and J. Janek, "Gas evolution in operating lithium-ion batteries studied in situ by neutron imaging." *Sci. Rep.*, **5**, 1 (2015).
30. B. Michalak, B. B. Berkes, H. Sommer, T. Bergfeldt, T. Brezesinski, and J. Janek, "Gas evolution in LiNi0.5Mn1.5O4/graphite cells studied in operando by a combination of differential electrochemical mass spectrometry, neutron imaging, and pressure measurements." *Anal. Chem.*, **88**, 2877 (2016).
31. D. Goers, M. Holzapfel, W. Scheifele, E. Lehmann, P. Vontobel, and P. Novák, "In situ neutron radiography of lithium-ion batteries: the gas evolution on graphite electrodes during the charging." *J. Power Sources*, **130**, 221 (2004).
32. C. Tötzke, N. Kardjilov, I. Manke, and S. E. Oswald, "Capturing 3D water flow in rooted soil by ultra-fast neutron tomography." *Sci. Rep.*, **7**, 6192 (2017).
33. C. Tötzke, N. Kardjilov, N. Lenoir, I. Manke, S. E. Oswald, and A. Tengattini, "What comes NeXT?—high-speed neutron tomography at ILL." *Opt. Express*, **27**, 28640 (2019).
34. A. Tengattini, N. Lenoir, E. Andò, B. Giroud, D. Atkins, J. Beaucour, and G. Viggiani, "NeXT-grenoble, the neutron and X-ray tomograph in grenoble." *Nucl. Instruments Methods Phys. Res. Sect. A Accel. Spectrometers, Detect. Assoc. Equip.*, **968**, 1 (2020).
35. D. S. Hussey, J. M. LaManna, E. Baltic, and D. L. Jacobson, "Neutron imaging detector with 2 μm spatial resolution based on event reconstruction of neutron capture in gadolinium oxysulfide scintillators." *Nucl. Instruments Methods Phys. Res. Sect. A Accel. Spectrometers, Detect. Assoc. Equip.*, **866**, 9 (2017).
36. P. Trtik, J. Hovind, C. Grünzweig, A. Bollhalder, V. Thominet, C. David, A. Kaestner, and E. H. Lehmann, "Improving the spatial resolution of neutron imaging at paul scherrer institut - the neutron microscope project." *Phys. Procedia*, **69**, 169 (2015).
37. A. Kaestner, B. Münch, P. Trtik, and L. Butler, "Spatiotemporal computed tomography of dynamic processes." *Opt. Eng.*, **50**, 123201 (2011).
38. T. Kohler, "A projection access scheme for iterative reconstruction based on the golden section." *Nucl. Sci. Symp. Conf. Rec. 2004*, Piscataway, NJ (IEEE) **6**, 3961 (2004).
39. J. M. LaManna, D. S. Hussey, E. M. Baltic, and D. L. Jacobson, "Improving material identification by combining X-ray and neutron tomography." *Proc. SPIE*, **1039104**, 1 (2017).
40. R. F. Ziesche et al., "4D imaging of lithium-batteries using correlative neutron and X-ray tomography with a virtual unrolling technique." *Nat. Commun.*, **11**, 11 (2020).

41. SAFT, "Data sheet—SAFT LS." 142501 (2009).
42. N. Kardjilov, A. Hilger, I. Manke, R. Woracek, and J. Banhart, "CONRAD-2: The new neutron imaging instrument at the Helmholtz-Zentrum Berlin." *J. Appl. Crystallogr.*, **49**, 195 (2016).
43. N. Kardjilov, A. Hilger, and I. Manke, "CONRAD-2: cold neutron tomography and radiography at BER II (V7)." *J. Large-Scale Res. Facil. JLSRF.*, **2**, 1 (2016).
44. J. Schindelin et al., "Fiji : an open-source platform for biological-image analysis." *Nat. Methods*, **9**, 676 (2012).
45. W. Kockelmann et al., "Time-of-flight neutron imaging on IMAT@ISIS: a new user facility for materials science." *J. Imaging.*, **4**, 47 (2018).
46. T. Minniti et al., "Materials analysis opportunities on the new neutron imaging facility IMAT@ISIS." *J. Instrum.*, **11**, C03014 (2016).
47. T. Minniti, K. Watanabe, G. Burca, D. E. Pooley, and W. Kockelmann, "Characterization of the new neutron imaging and materials science facility IMAT." *Nucl. Instruments Methods Phys. Res.*, **888**, 184 (2017).
48. W. van Aarle, W. J. Palenstijn, J. Cant, E. Janssens, F. Bleichrodt, A. Dabravolski, J. De Beenhouwer, K. Joost Batenburg, and J. Sijbers, "Fast and flexible X-ray tomography using the ASTRA toolbox." *Opt. Express*, **24**, 25129 (2016).
49. W. van Aarle, W. J. Palenstijn, J. De Beenhouwer, T. Altantzis, S. Bals, K. J. Batenburg, and J. Sijbers, " The ASTRA Toolbox: a platform for advanced algorithm development in electron tomography." *Ultramicroscopy*, **157**, 35 (2015).
50. A. N. Dey, "S.E.M. studies of the Li-film growth and the voltage-delay phenomenon associated with the lithium-thionyl chloride inorganic electrolyte system." *Electrochim. Acta*, **21**, 377 (1976).